# Supplementary Material: Machine Learning Based Prediction of Polaron-Vacancy Patterns on the TiO$_2$(110) Surface

Viktor C. Birschitzky,[*,†] Igor Sokolović,[‡] Michael Prezzi,[†] Krisztián Palotás,[¶]
Martin Setvín,[§,‡] Ulrike Diebold,[‡] Michele Reticcioli,[†] and Cesare Franchini[†,‖]

†Faculty of Physics and Center for Computational Materials Science, University of Vienna, Vienna, Austria

‡Institute of Applied Physics, TU Wien, Vienna, Austria

¶Institute for Solid State Physics and Optics, HUN-REN Wigner Research Center for Physics, Budapest, Hungary

§Department of Surface and Plasma Science, Faculty of Mathematics and Physics, Charles University, Prague, Czech Republic

‖Dipartimento di Fisica e Astronomia, Università di Bologna, Bologna, Italia

E-mail: viktor.birschitzky@univie.ac.at
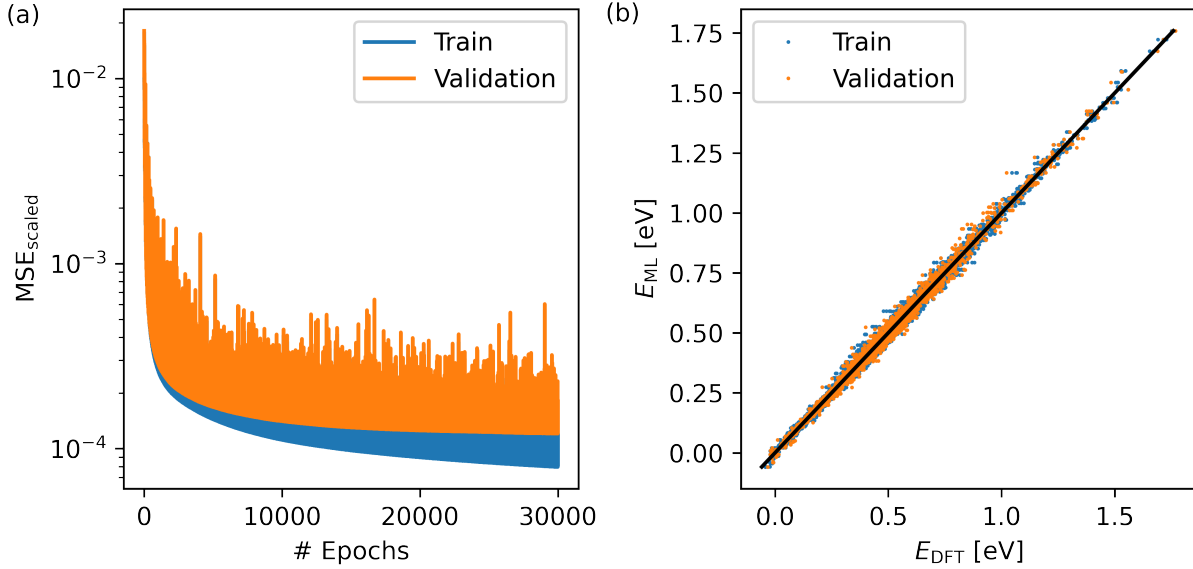
1

# 1 Machine Learning Model Training
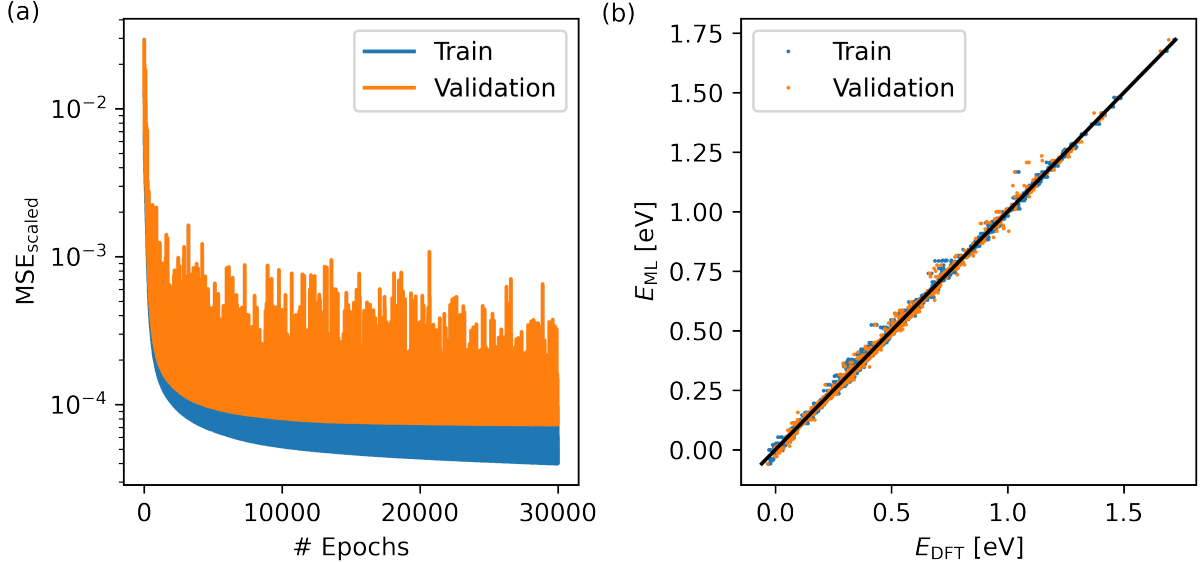


Supplementary Figure 1: Training procedure of the 6×4 model characterized with a (a) learning curve and a (b) scatter plot comparing DFT- and ML-based energies.

# 2 Exhaustive $V_O$-configurations in the 6×4-cell

During the active learning scheme, we exhaustively predicted optimal polaron configurations in all possible oxygen vacancy configurations in the $6 \times 4$-cell. Figure 5 shows the energy distribution of the most favorable configurations as predicted by the ML model. The marked region at the lowest energies shows the most interesting configurations and is comprised of all configurations that feature one oxygen vacancy per [001] bridging oxygen row. Less stable configurations were not explored as thoroughly during active learning and might contain less accurate predictions, or some configurations, which were not reproducible at the DFT level.

In Figure 6, we collect the best polaron configuration for all $V_O$-configurations in the low energy cluster, with their respective DFT energy. Figure 7 collects the energy changes due to different treatments of polaron-defect interaction in the low energy $V_O$ configuration

2

Supplementary Figure 2: Training procedure of the combined 6×4 and 12×2 model characterized with a (a) learning curve and a (b) scatter plot comparing DFT- and ML-based energies.

cluster. Some notable features here are the presence of $Ti_{S0}$-polarons (marked in orange) as compared to the reference dataset, where most stable configurations usually only consisted of $Ti_{S1}$-polarons (marked in yellow). The presence of $Ti_{S0}$-polarons is usually associated with two oxygen vacancies aligned along $[1\bar{1}2]$ or $[1\bar{1}0]$, which stabilizes the excess charge at a surface $Ti_{5c}$ site. Subsurface polarons are most stable in the homogeneous ground state, in particular, when placed symmetrically and diagonally aligned between two oxygen vacancies in adjacent rows.
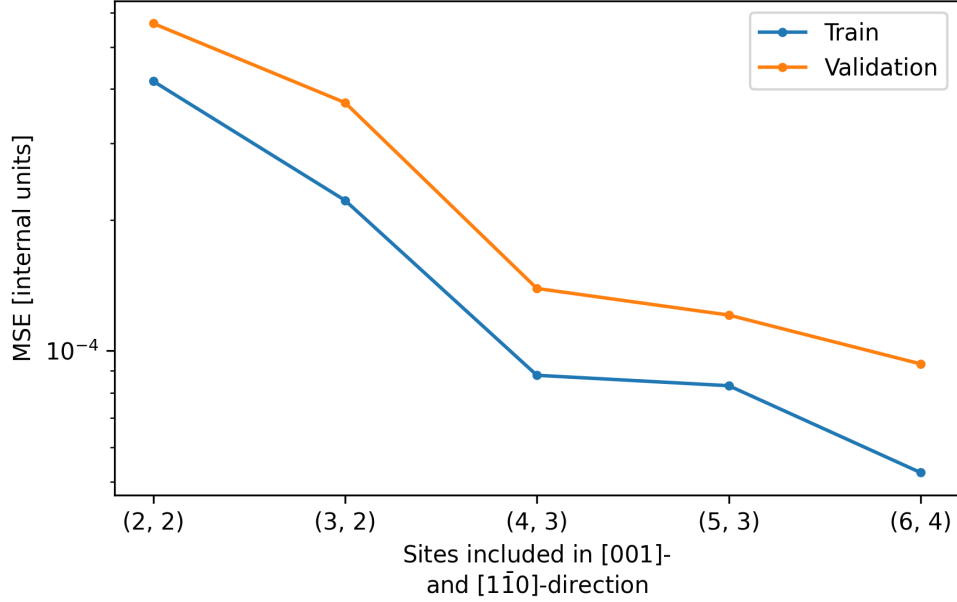
Supplementary Figure 3: Model MSE after 10000 epochs of training in dependence of the cutoff region around each defect.

# 3 Experimental Autocorrelation Function

To quantify the attraction and repulsion of $V_O$s on the rutile $TiO_2(110)$ surface, we calculated the autocorrelation function of $V_O$ positions as extracted by STM measurements. First, we identified the $V_O$ positions in the STM image (Figure 8a). Then, we calculated the average number of $V_O$s around each detected $V_O$ position. This was done by overlaying copies of the $V_O$ positions on top of each other, such that each $V_O$ was placed at the origin once (Figure 8b). The resulting grid-like distribution was subdivided into individual grid cells, and the number of $V_O$s in each cell was counted.
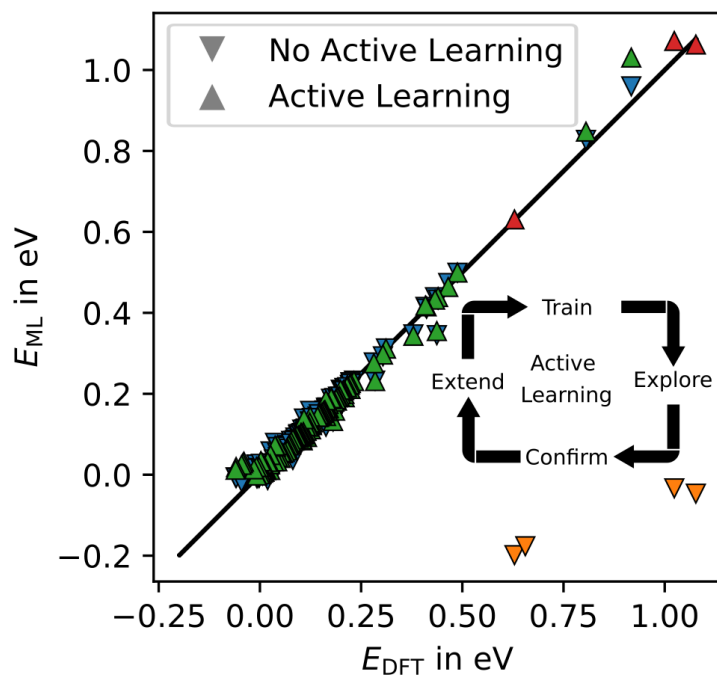
Supplementary Figure 4: Comparison of test-set predictions for the model with (up-pointing triangles) and without (down-pointing triangles) iterative active learning. Blue and green data points were not added to the training data, orange and red have been used to extend training data. The inset schematically displays the active learning loop
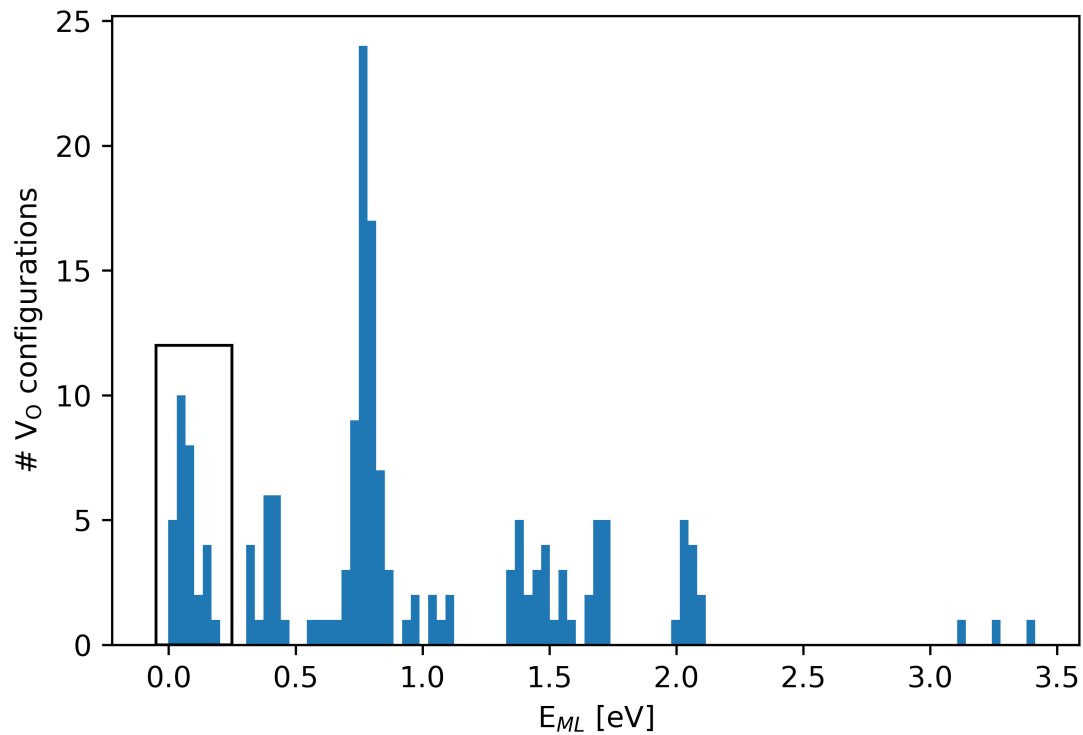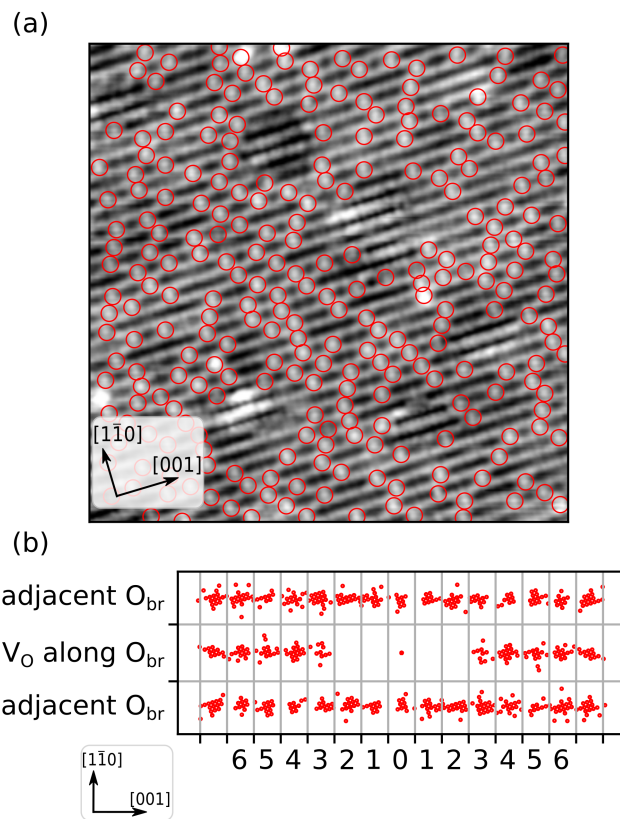
Supplementary Figure 5: Distribution of ML-predicted lowest energies within all possible $V_O$-arrangements in the $6 \times 4$-cell. Only energies of the optimized polaronic structure for each $V_O$-configuration are displayed. The highlighted cluster in the bottom left corresponds to the in-depth optimized configurations displayed in Figure 6.
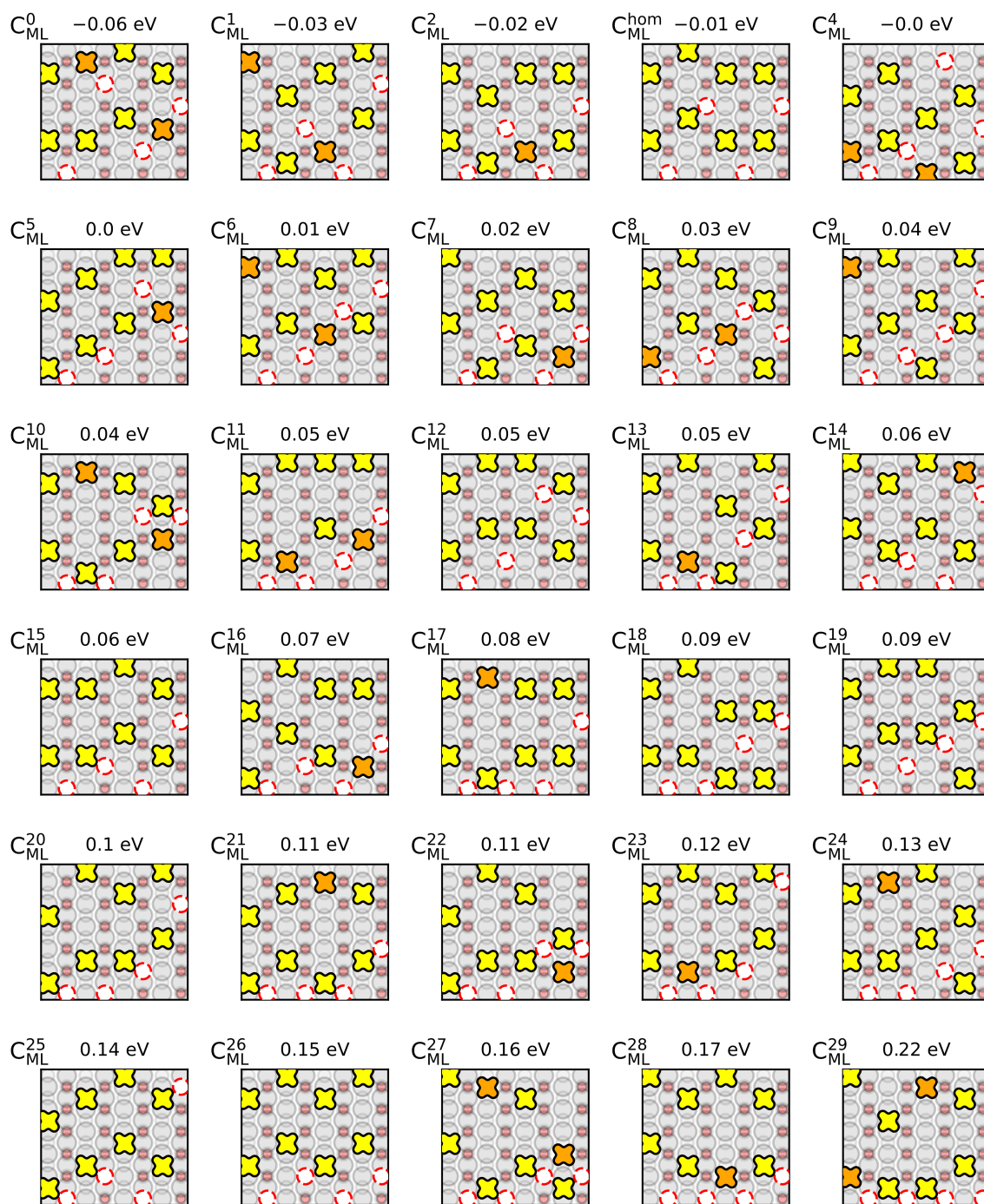
Supplementary Figure 6: Schematic representation of the ML-determined optimal polaron-$V_O$ configuration. The 30 most stable $V_O$-configrutions are displayed as determined by simulated annealing of the polaron configuration in a fixed $V_O$-configuration. $V_O$ are displayed as dashed red circles, surface polarons in orange, and subsurface polarons in yellow. The DFT energies are given relative to the random polaron homogeneous $V_O$ distribution. The number in the label indicates the stability rank.
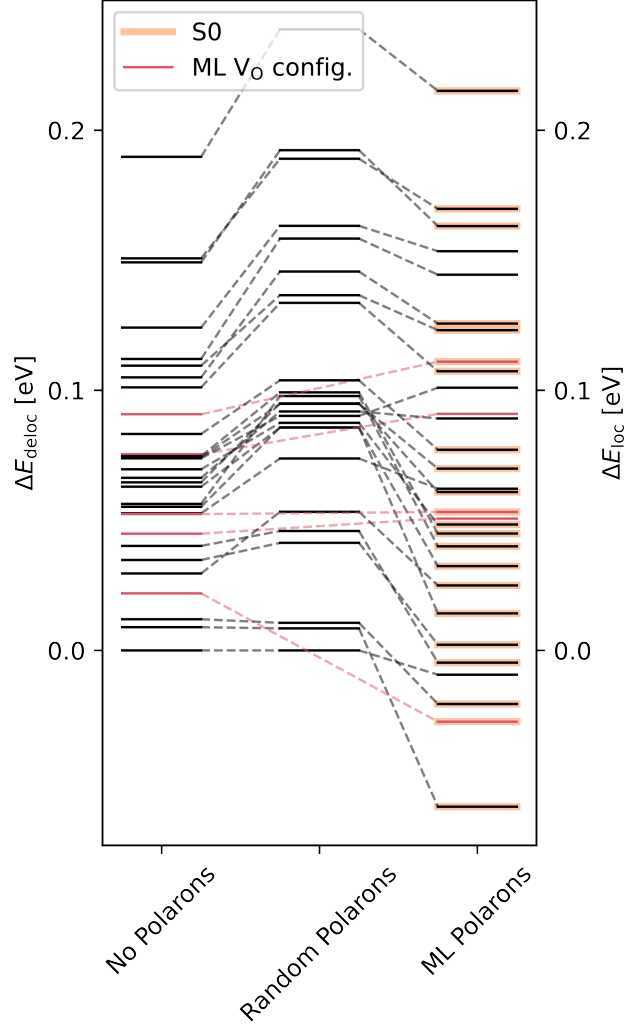
Supplementary Figure 7: Changes of energies for all $V_O$ configurations in the low energy cluster by different treatments of polaron-defect interactions. The ML Polarons column corresponds to the configurations displayed in Figure 6, where the most stable configuration in the bottom of the ML Polarons column is $c_{ML}^0$ and the highest energy level belongs to $c_{ML}^{29}$. The other configurations are labeled sequentially. Configurations containing S0 polarons are highlighted in orange. The left energy scale $\Delta E_{deloc}$ labels the No Polarons column. The other two polaronic columns are labeled by the right energy scale $\Delta E_{loc}$.

(a)

[1̄10]
[001]

(b)

adjacent $O_{br}$

$V_O$ along $O_{br}$

adjacent $O_{br}$

[1̄10]
[001]

6 5 4 3 2 1 0 1 2 3 4 5 6

Supplementary Figure 8: Experimental autocorrelation function as extracted from Fig. 1b. (a) Detected $V_O$ positions marked by red circles in STM measurement. (b) Experimental autocorrelation function of the $V_O$ positions along a single and in the adjacent [001]-aligned $O_{br}$ rows.